Design and first application of a novel laboratory reactor for alkali studies in chemical looping applications

Fuel Processing Technology 252 (2023) 107988

Contents lists available at ScienceDirect

Fuel Processing Technology

journal homepage: www.elsevier.com/locate/fuproc

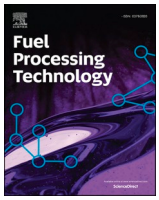

Design and first application of a novel laboratory reactor for alkali studies in chemical looping applications

Viktor Andersson [a], Xiangrui Kong [a], Henrik Leion [c], Tobias Mattisson [b], Jan B.C. Pettersson [a,*]

[a] Department of Chemistry and Molecular Biology, Atmospheric Science, University of Gothenburg, Medicinaregatan 7B, SE-413 90 Gothenburg, Sweden
[b] Department of Space, Earth and Environment, Division of Energy Technology, Chalmers University of Technology, Hörsalsvägen 7A, SE-412 96 Gothenburg, Sweden
[c] Energy and Materials, Chemistry and Chemical Engineering, Chalmers University of Technology, Kemigården 4, SE-412 96 Gothenburg, Sweden

ARTICLE INFO

Keywords:
Oxygen carrier
Chemical looping combustion
Alkali
Laboratory reactor

ABSTRACT

Alkali compounds are readily released during biomass conversion and their complex interactions with reactor walls and sampling equipment makes detailed investigations challenging. This study evaluates a novel laboratory-scale fluidized bed reactor for chemical looping combustion (CLC) studies. The reactor design is based on detailed consideration of the behavior of alkali-containing molecules and aerosol particles and is guided by computational fluid dynamic simulations. The design allows for interactions between gaseous alkali and a fluidized bed, while minimizing alkali interactions with walls before and after the fluidized bed. The function of the laboratory reactor is demonstrated in experiments using online gas and alkali analysis. Alkali is continuously fed to the reactor as KOH or KCl aerosol with and without a fluidized bed of the oxygen carrier $CaMn_{0.775}Ti_{0.125}Mg_{0.1}O_{3-\delta}$ present in inert, reducing and oxidizing conditions at temperatures up to 900 °C. Alkali uptake by the OC is characterized in all conditions, and observed to sensitively depend on gas composition, reactor temperature and type of alkali compound. The experimental setup is concluded to have a significantly improved functionality compared to a previously used reactor, which opens up for detailed studies of interactions between alkali compounds and oxygen carriers used in CLC.

1. Introduction

Implementation of biomass combustion for heat and power generation has the potential to significantly reduce greenhouse gas emissions and other harmful pollutants, and thus represents a key factor in mitigating global warming. Converting biomass in a chemical looping combustion (CLC) system provides the possibility of reaching negative CO_2 emissions [1,2]. The CLC technology is based on two interconnected fluidized bed reactors: an air reactor (AR) that operates under oxidizing conditions and a fuel reactor (FR) that operates under reducing conditions, and solid oxygen carrier (OC) particles that circulates between the two reactors [3]. Although solid biomass can be converted in a CLC system, the combustion of biomass fuels generally impose several challenges. In comparison to fossil fuels, biofuels generally have a lower heating value, a higher water content and often contain aggressive ash components, such as the alkali metals potassium and sodium [4]. Biomass used for combustion generally contains between 0.1 and 1.1 wt % alkali on a dry fuel basis [5]. The alkali, which is readily released during the conversion process, is volatile at temperatures exceeding 700 °C and can be transported between fuel particles and fluidized bed particles [6,7]. Alkali compounds may cause detrimental problems to the system equipment and reduce overall efficiency. Some typical problems that may arise are fouling and corrosion of process equipment [4,8–10], interaction with the oxygen carrying bed material [11,12] and fluidization disturbances due to bed agglomeration [8,13,14]. However, alkali metals are often used as promoters in catalytic reactions, and studies show that they have catalytic effects on carbon conversion [15], tar cracking [16,17] and char reactivity [18–21]. Several studies have investigated the positive effects of alkali during gasification. Increasing K content in different types of biomass has been shown to increase gasification reactivity [22,23], and a high K/C ratio in biomass increases the gasification rate during CO_2 gasification [24,25].

The significant effects of alkali compounds in thermal conversion systems have led to extensive research in the field. There have been studies of the interaction between alkali and the OC [11–13,26,27] and studies focusing on gaseous alkali components in the exhaust gases [5,28,29]. Reactors ranging from industrial scale [28,30,31] to laboratory scale [29,32–34] have been employed in the research. However, the

* Corresponding author.
E-mail address: janp@chem.gu.se (J.B.C. Pettersson).

https://doi.org/10.1016/j.fuproc.2023.107988
Received 17 August 2023; Received in revised form 6 October 2023; Accepted 18 October 2023
Available online 31 October 2023

complex behavior of alkali makes it challenging to gain detailed knowledge of the interactions in thermal conversion systems. Studies in large-scale facilities generally rely on extractive sampling where deposition and condensation on surrounding surfaces and chemical transformations may be important. Systematic studies of thermal conversion processes like CLC often use reactors on laboratory-scale to lay the scientific foundation and complement pilot- and industrial-scale studies. However, detailed interactions between alkali and the component of interest, *e.g.,* oxygen carriers, might be obscured if the surrounding reactor walls cause significant effects. Compared to large-scale facilities, the laboratory-scale reactors generally have a larger surface-to-volume ratio and higher wall temperatures due to external heating [32]. Furthermore, steel is often used as reactor wall material in alkali studies on laboratory-scale [29,32,35–37], and studies related to CLC often apply conditions that alternate between oxidizing and reducing atmospheres. Alternating atmospheres in the presence of alkali may change the elemental composition of the gaseous alkali, but also the chemical and physical behavior of the high temperature steel walls and thereby affect their interactions with alkali [32].

Previous studies employed a stainless steel fluidized bed reactor on laboratory-scale to characterize the interactions between alkali and reactor walls [32], and the interactions between alkali and a fluidized bed of synthetic calcium manganite OC [29]. Alkali aerosol particles were continuously fed to the reactor in oxidizing, inert and reducing conditions at temperatures up to 900 °C, while the alkali concentration was measured online in the exhaust gas. When temperatures exceed 500 °C, the alkali particles rapidly evaporate to their molecular constituents, resulting in greatly increased diffusion towards the surrounding surfaces. The alkali-wall interactions were influenced by the atmospheric conditions, with significant transients in alkali outlet concentrations when shifting between reducing, inert and oxidizing gas environments. It was suggested that the strong dependence on the gas phase correlates to changes in the properties of the outermost reactor wall surface which is in contact with the gas inside the reactor [32]. Although providing valuable information about alkali interacting with the OC, the study clearly showed the need for improved experimental methodology considering the significant interactions between the laboratory reactor and the gas phase alkali [29].

This study presents the development of a novel fluidized bed reactor, designed for laboratory-scale alkali studies under conditions relevant to CLC. The design is based on fundamental understanding of aerosol processes and computational fluid dynamics (CFD) simulations, and a stainless steel material with excellent corrosion resistance is chosen as the wall material. The overall aim with the new design is to limit alkali losses below and above the fluidized bed, allowing for detailed studies of the interactions between alkali and a fluidized bed of OC particles. The function of the new reactor is demonstrated with typical CLC experiments.

2. Design of a novel laboratory reactor

2.1. Design considerations

Our previous work illustrates the challenges in studying alkali processes on the laboratory scale [29,32]. Alkali in the form of aerosol particles can be transported in a controlled way and with limited losses in low temperature tubes to and from a laboratory reactor [38]. When the temperature exceeds the evaporation point of the aerosol particles, the alkali compounds will exist in their gaseous state with diffusion coefficients several orders of magnitude higher compared to aerosol particles. Alkali in molecular form may therefore rapidly diffuse to and interact with hot surfaces in the vicinity, including OC particles, reactor walls and gas extraction probes. Additionally, these interactions may be influenced by the surrounding gas conditions, temperature and the elemental composition of the alkali species. When the temperature drops, the alkali will either condense onto cold surfaces or nucleate and form new aerosol particles [39]. The size of the formed aerosol particles depends on the mass concentration of alkali in the gas flow. The particles grow over time due to further condensation of gas-phase alkali compounds and agglomeration of aerosol particles [38]. The diffusion coefficient of the formed particles is several orders of magnitude lower than that of alkali in gaseous form [29], and the particles are efficiently transported to the measurement equipment with limited losses to tube walls [38].

A reactor with a simple geometry was previously used for alkali studies in CLC. It consisted of a 960 mm long vertical tube with an inner diameter of 26 mm, and a 600 mm long central part of the reactor was heated by an external furnace [29,32]. The reactor contained a fluidized bed situated above a perforated plate in the heated zone of the reactor. One problem with this reactor design was the extended hot regions above and below the fluidized bed where alkali in gaseous form could interact with the hot reactor walls [29]. Alkali-wall interactions upstream and downstream of the OC bed thus affected the alkali concentrations making it difficult to separate the effects of alkali-OC and alkali-wall interactions.

In this study, a new reactor design is developed that limits the alkali losses before and after the fluidized bed. The main design ideas are presented here before describing the detailed design in subsequent sections. The new setup can be separated into three main sections: a gas and alkali inlet section below the fluidized bed, a hot middle section including the fluidized bed, and a third section with lower temperatures downstream of the fluidized bed including the exhaust gas outlet.

In the first section, alkali aerosol particles suspended in nitrogen is introduced at room temperature through a narrow tube in the center of the reactor body, which exits just before the fluidized bed. A narrow tube diameter results in a high gas velocity and short residence time of the gas, which allows the aerosol flow to remain relatively cold. Therefore, the alkali remains as aerosol particles before entering the fluidized bed, despite the fact that the final part of the aerosol tube is located within the heated section of the reactor.

To maintain sufficient operating temperature in the fluidized bed, a separate flow of reactor gases is preheated to near operating temperature before entering the main reactor body. In addition, the reactor gas inlet is connected tangentially to the main reactor body to produce a swirling motion of the pre-heated gas inside the reactor. The reactor gas is swirling around the centered aerosol flow, limiting alkali transport to the main reactor walls. This configuration of the inlet section should limit aerosol particle evaporation below the bed, and keep the alkali flow separated from the main reactor walls while still producing an even temperature of the fluidized bed. Consequently, alkali interactions with the reactor walls below the bed should be considerably lower in the new reactor design compared to the previous reactor.

Another significant difference from the previous reactor [29,32], is that the heated second section of the new reactor is less than half the height of the old one. This removes a major part of the hot wall surface where no fluidized bed is present, which results in overall less alkali-wall interactions. Furthermore, alkali studies in thermal conversion systems on laboratory-scale generally employ reactors of stainless steel alloys where iron and chromium oxides dominate the surface layer of the walls [40,41]. At high temperatures, alkali can react with these oxide layers to form products, including K_2CrO_4 and $K_2Fe_2O_4$ [42,43]. Therefore, the hot sections of the new reactor should be manufactured in a steel material which forms stable oxide layers that limit chemical reactions with alkali.

The third section of the reactor downstream of the fluidized bed is characterized by a significantly increased diameter compared to the preceding fluidized bed section. This section has no external heating and the increase in reactor diameter improves the cooling of the gas exiting the fluidized bed by increasing the residence time, while also reducing the surface-to-volume ratio. The rapid quenching of the hot gas leaving the fluidized bed when entering the third section results in efficient formation of new aerosol particles that may be efficiently transported to

downstream on-line instruments [38]. Another benefit of the increased reactor diameter is a lowered gas velocity, which makes it less likely that fluidized bed OC particles are carried away by the gas stream.

2.2. CFD simulations

CFD simulations were employed to optimize the geometric configuration of the laboratory reactor regarding the behavior of alkali aerosol particle characteristics at the relevant temperatures. The CFD simulation was performed with the ANSYS Fluent 2021 R2 software, which is widely used in the CFD community [44–46]. A pressure-based segregated algorithm where the pressure-velocity coupling is solved with the SIMPLEC scheme was chosen to solve the Navier-Stokes equations [47,48]. This scheme was chosen since it can reach a converged solution more quickly compared to other schemes for relatively uncomplicated problems. For more complicated problems where turbulence or additional physical models are applied it is more likely that one of these models limits the convergence, and different schemes give similar results [48]. In addition, second order upwind schemes were applied for the spatial discretization. The simulation used a steady state solver with a two-equation eddy-viscosity sheer stress transport (SST) k-ω turbulence model and surface to surface (S2S) radiation enabled. Radiation was not applied to OC particles, and the exothermic and endothermic reactions of the OC that would take place in oxidizing and reducing conditions, respectively, were not included in the simulation. Since the movement of a fluidized bed requires transient simulation, and the heating of the reactor and bed is a comparably slow process, the CFD simulation was performed with a steady state solver where the fluidized bed is realized as a porous fixed bed. The thermodynamic properties of the bed were similar to those for the stainless steel wall, the height of the bed was set to 10 cm and a void fraction of 0.5 was used.

The boundary conditions for the inlets were set to room temperature with a specified velocity magnitude normal to the boundary of 1.3 m s^{-1} (1 L min^{-1}) for the aerosol flow and 0.398 m s^{-1} (0.3 L min^{-1}) for the reactor gas flow. The outlet boundary was defined as pressure outlet. The boundary conditions for the walls were set to stationary walls with no slip shear condition. All walls were defined as steel with a constant density of 7250 kg m^{-3}, a specific heat capacity of 680 J kg^{-1} K^{-1} and a thermal conductivity of 25 W m^{-1} K^{-1}. Radiation was defined with an internal emissivity of 0.7 while the thermal conditions depend on the location of the wall. Walls in the section with ambient outer temperatures were defined by a convective thermal condition with a 6 W m^{-2} K^{-1} heat transfer coefficient and a 26 °C free stream temperature. Walls within the heated section of the furnace were subjected to a constant heat flux 1820 W m^{-2} at an operating temperature of 900 °C. The insulated wall sections were subjected to a constant heat flux of 0 W m^{-2}.

A convergence criteria of 10^{-6} was applied to all residuals except continuity, where 10^{-5} was used. A mesh was generated from an automated meshing software, and a grid independency test was performed to ensure reliable results. The test was based on changing the number of elements in the mesh from approximately $0.1{\cdot}10^{-6}$ to $0.7{\cdot}10^{-6}$ in seven steps. The parameters that were monitored during the test were temperature and velocity below the bed, above the bed and in the outlet. It was seen that the results changed by less than 2% when the number of elements in the mesh exceeded $0.5{\cdot}10^{-6}$. The final mesh had a minimum and average orthogonal quality of 0.33 and 0.92, respectively, and a maximum and average skewness of 0.67 and 0.15, respectively.

The CFD simulation was an iterative process where the geometry of different reactor parts, the gas flow rates and the properties of heating and cooling were manually changed in several step until an optimal design was established. The inlet configuration and flow rates of aerosol and reactor gas were optimized to: *i*) keep a sufficiently low temperature of the aerosol flow to limit alkali losses to surrounding walls below the fluidized bed, *ii*) allowing rapid aerosol particle evaporation upon entering the bed, and *iii*) maintain the operating temperature throughout the fluidized bed.

The size of the heated section was designed to limit the area of hot reactor walls downstream of the fluidized bed, while still providing sufficient heat flux. The dimensions were adjusted slightly after consultation with a furnace provider. The diameter and height of the section downstream of the furnace was adjusted to reach rapid temperature quenching and limit alkali condensation onto cold walls. This section was also adjusted slightly after consultation with the reactor manufacturer.

Fig. 1 shows the final CFD modelling results from the optimal reactor design when the reactor was simulated to operate at 900 °C where the 1 L min^{-1} aerosol flow and the 0.3 L min^{-1} reactor gas flow consisted of pure N_2 with temperature dependence according to the ideal gas law. The heating of the reactor was simulated by applying a constant heat flux onto the outer reactor walls in the simulation. The fluidized bed, the heated section, the aerosol nucleation section, inlets and outlet are annotated in the figure.

Fig. 1a shows the temperature profile of the inner reactor walls and corresponding temperature gradients in the flow path inside the reactor are shown in Fig. 1b-c. Previous experiments using an alkali aerosol generator concluded that 45 nm KCl aerosol particles evaporate around 500 °C, leading to greatly increased diffusion coefficients and increased alkali-wall interactions [32]. Fig. 1b shows that the majority of the aerosol flow is kept below 400 °C before reaching the fluidized bed. As the alkali-containing aerosol particles enter the bed, the temperature rapidly increases above the evaporation point, allowing gaseous alkali to interact with the solid bed particles. Fig. 1a and c show the configuration of the reactor gas inlet, where the gas is preheated in a tube that runs alongside the main reactor body inside the furnace.

Cross-section profiles of temperature and velocity at the inlet point of reactor gases are shown in Fig. 1d and e. The reactor gas inlet is positioned with a 10 mm offset from the center of the reactor body, *i.e.,* tangential to the circular reactor wall. This way, the reactor gas will flow in a swirling, circular, motion when it enters the reactor, which improves the distancing between the centered alkali aerosol flow and the reactor walls. The configuration allows the temperature of the aerosol flow to remain below the evaporation point of aerosol particles while the surrounding reactor gases have been preheated to maintain sufficient temperature of the fluidized bed. Additional CFD simulations was performed with 2 and 4 reactor gas inlets, positioned tangentially with the reactor body. This did not make significant changes to either the reactor gases, aerosol gases or temperature profiles, which is why a single reactor inlet was chosen to simplify the geometry. The temperature profile in Fig. 1d ranges between 400 and 850 °C, *i.e.,* the blue fields mark areas where the temperature is below the evaporation point of the alkali particles. Important to note is that immediately before the aerosol flow exits the tube, approximately 40% of the gas exceeds a temperature of 500 °C. However, the high gas velocity in the tube result in a gas residence time below 3 ms in this region, and the alkali is assumed to remain as aerosol particles inside the narrow tube.

The section without external heating downstream of the furnace is characterized by an increase in reactor diameter that effectively quenches the temperature and reduces the surface-to-volume ratio in this part of the reactor, see Fig. 1b. The results in the figure illustrate that the temperature of the gas flow is below 200 °C before exiting the reactor.

Additional CFD simulations were performed with different oven sizes and operating temperatures. Increasing the length of the heated section from 200 to 300 mm (*i.e.,* increasing the heated area) requires an overall lower heating effect (W) to produce the same total heat flux (W/m^2). This, however, leads to less efficient heating of the inlet section and colder regions in the bottom of the fluidized bed. The topmost regions of the bed is warm, along with extensive hot wall areas above the fluidized bed. To limit alkali losses above the bed, and to maintain sufficient bed temperature, it is more beneficial to use a smaller (200 mm) furnace operated with higher heating effect. Changing the operating

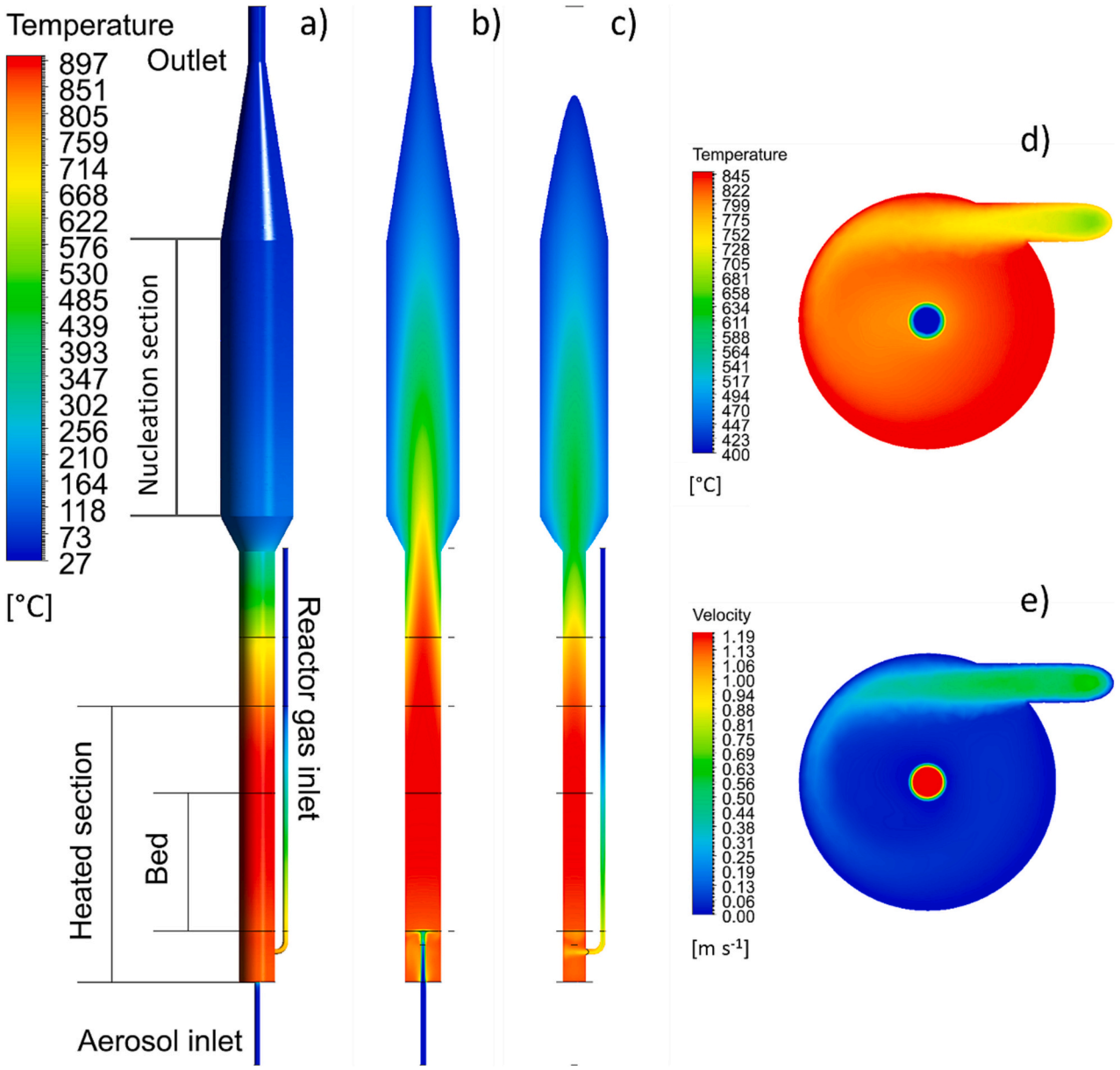

Fig. 1. Results from CFD calculations showing temperature profiles of the (a) inner surface of the reactor steel walls, (b) cross section of the flow path in the center of the reactor and (c) cross section of the flow path in the center of the reactor gas inlet tube. (d) Temperature profile and (e) velocity profile over the cross section of the reactor body at the reactor gas inlet.

temperature in the range from 600 to 1000 °C did not cause major changes in the gas temperature exiting the reactor. This is due to the relatively long residence time of the outlet gases in the top section of the reactor with ambient outer temperature, in combination with efficient cooling rates. The relevant temperatures for aerosol nucleation are above a few hundred degrees, and these temperatures are rapidly reached in the section without external heating. The reactor operating temperature, however, affects the temperature of the inlet section to a greater extent. At the lowest (600 °C) temperature, the low temperatures of the aerosol and reactor gases cause significant cooling in the bottom regions of the fluidized bed. At the higher temperatures (800–1000 °C), the bed maintains a sufficient operation temperature.

Additional CFD simulations using the same methodology were carried out for the previously used reactor [29,32]. Fig. 2 compares the temperature profiles within the new and previously used reactor setups, where the old reactor consists of a long cylindrical tube with a centrally heated section. Note that the fluidized bed positions in Fig. 2 correspond to the positions of the porous beds used in the simulations, while an actual fluidized bed would extend further with a zone with decreasing bed density towards the outlet. The old reactor exhibits extensive regions of high temperature both above and below the fluidized bed in the central heated section. On the inlet side, a large fraction of an injected alkali aerosol will experience high temperatures before reaching the fluidized bed. This results in alkali salt evaporation and rapid diffusion of alkali-containing compounds to the reactor wall. The alkali flow reaching the fluidized bed is thereby strongly affected by alkali-wall interactions. A similar situation exist after the fluidized bed, where alkali compounds leaving the bed have a high probability of interacting with the hot wall before escaping from the reactor. In contrast, these problems are significantly reduced by the optimized designs of the inlet and outlet regions in the new reactor. Another issue in the old reactor is the temperature gradient within the central part containing the bed. Conversely, the new reactor showcase a more uniform temperature distribution within the hot zone housing the fluidized bed. This

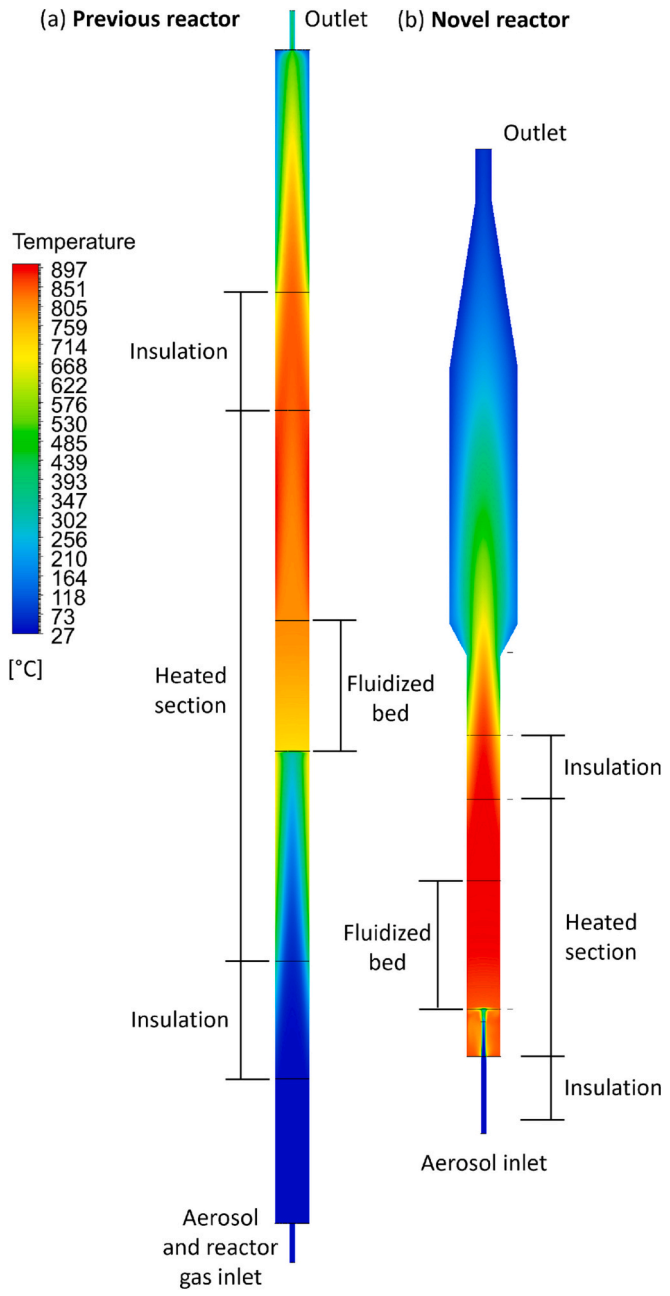

Fig. 2. Results from CFD simulations showing temperature profiles of the (a) cross section of the flow path in the center of the novel reactor, and (b) cross section of the flow path in the center of the reactor used in previous studies.

improved uniformity can be attributed primarily to the gas preheating implemented in the new reactor.

2.3. Reactor construction

The new laboratory-scale fluidized bed reactor was constructed based on the design considerations and CFD simulations described above, and the geometry and dimensions of the reactor are schematically shown in Fig. 3. The color scheme in the figure shows the heated area (red), insulated areas (green) and areas without insulation experiencing ambient temperatures (blue). Fig. 3a shows the produced reactor before any experiments were carried out and Fig. 3b shows the geometric configuration of the reactor assembly with dimensions in mm. Marked in the figure is also the flow direction of the aerosol, reactor gases and exhaust gas. Fig. 3c shows the location of aerosol and reactor gas inlets (transparent red color) in relation to the fluidized bed (solid red color). Fig. 3d shows a cross section of the reactor body near the aerosol and reactor gas inlets. The reactor gases enter in the tangential direction of the reactor body while the aerosol inlet tube is located in the center. The reactor section with ambient temperature includes a seemingly long distance with 26 mm inner diameter, which is contradictory when aiming to limit the area of reactor walls. The reason is that this section includes a flange, which makes it possible to remove or change the upper reactor section (*i.e.,* the blue section in Fig. 3b). The size of the 26 mm diameter section with ambient temperature could have been reduced if the sections were welded instead of connected with flanges.

A particle filter for the fluidized bed made of stainless steel (alloy 316) works as a gas distributor plate (see Fig. 3c). The sections shown in red and green in Fig. 3b and the associated flange (Fig. 3a) are made of a corrosion-resistant steel material, while the section and flange experiencing ambient outer temperatures (blue areas in Fig. 3b) are made of stainless steel (alloy 316). Due to the highly corrosive environment, it was crucial to build the hot parts of the reactor wall in a material with high corrosive resistance. The material used for these parts are Kanthal APMT™ (Sandvik AB). It is a powder-metallurgical ferritic Fe-Cr-Al alloy with an addition of Mo, which forms a stable surface oxide of non-scaling α-Al_2O_3 with good protection in corrosive high temperature environments. The main advantage is that the alumina oxide does not evaporate and the ionic diffusivity is low compared to Cr_2O_3, which is the main oxidation product of lower grade stainless steel alloys [49]. The downside of the APMT steel is its fragile properties at room temperature, and tightening of flanges and pipe fittings need to be done with care.

The reactor was operated at 900 °C in an oxidizing atmosphere for several hours without the addition of alkali before the first experiment was conducted. The pre-oxidation is expected to result in the formation of an oxide layer on the steel material that should be stable during regular redox studies included in this paper.

3. Experimental methodology

The experimental setup for the evaluation of the new fluidized bed reactor is displayed in Fig. 4, where the laboratory-scale reactor is externally heated by an electrically heated furnace. The experimental setup enables easily adjustable and stable concentrations of alkali and reactor gases introduced to a fluidized bed of OC particles while gas and alkali concentrations are monitored online with high time resolution in the exhaust. The alkali, produced by an aerosol generator (Model 3076, TSI Inc.), is fed from the bottom of the reactor assembly. An automated gas feeding system controls the gas atmosphere conditions. A gas analyzer and a surface ionization detector (SID) provide online measurements of gas and alkali concentrations in the exhaust gases. Similar experimental setups have been used in earlier studies [29,32].

The alkali was fed in the form of KOH or KCl aerosol particles with an average diameter of 45 nm dispersed in a 1 L min^{-1} nitrogen flow. A detailed description of the alkali aerosol generation process can be found elsewhere [32]. The 1 L min^{-1} aerosol flow was mixed with 0.3 L min^{-1} reactor gases before entering the fluidized bed to resemble the inert, reducing and oxidizing environments of a CLC system. The reactor gases consisted of either N_2, synthetic fuel gas (50% H_2 in CO) or synthetic air (21% O_2 in N_2), which after gas mixing resulted in 5.4 mg m^{-3} KOH or KCl in 1.3 L min^{-1} of either pure N_2, 11.5 vol% H_2 and 11.5 vol% CO in N_2 or 4.8 vol% O_2 in N_2.

The gas leaving the reactor is divided into three different streams; one leading through a diluter to an alkali detector, one through a condenser and particle filter to a gas analyzer and the excess gas is directed to the ventilation. The sample gas was diluted 10 times with N_2 before entering the SID which measured the total alkali concentration with a time resolution of 1 s. A detailed description of the SID technique is reported elsewhere [28,50–52] and the instrument has been used in several combustion related studies previously [5,28–30,32,53,54].

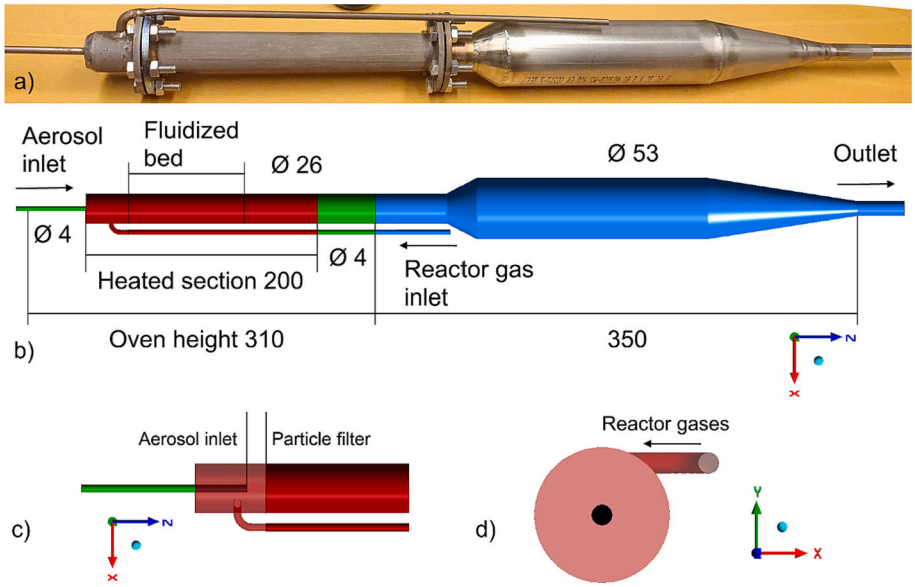

Fig. 3. Schematic overview of the laboratory-scale fluidized bed reactor with dimensions in (mm). Red fields mark heated areas, green fields mark insulated areas and blue fields mark ambient temperature areas. (For interpretation of the references to color in this figure legend, the reader is referred to the web version of this article.)

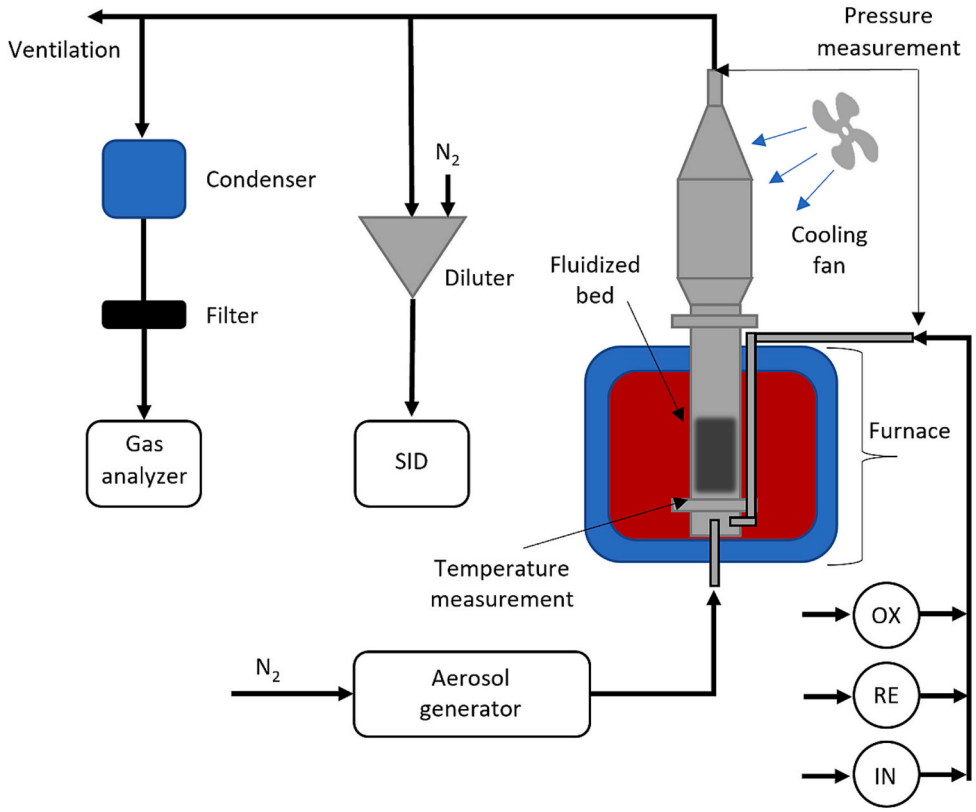

Fig. 4. Schematic of the laboratory reactor, externally heated by an electric furnace. An aerosol atomizer generates alkali aerosol that is fed through a 6 mm tube from the bottom of the reactor. An automated valve system regulates the environmental gases, which are preheated along the reactor body and fed to the bottom of the reactor. A fan provides additional cooling to the ambient section in the topmost reactor parts. The outlet is fed to a gas analyzer and an alkali measurement system (SID).

Alkali-containing compounds nucleate to form aerosol particles in the cold section downstream of the fluidized bed and the particles are subsequently transported to the SID, which is optimized to detect alkali in particulate form [52]. The gas analyzer (Model NGA 2000, Emerson Electric Co.) measured the concentrations of O_2, CO_2, CO, H_2 and CH_4.

The reactor was filled with 5, 10 or 20 g of calcium manganite OC particles in the fluidized bed experiments. The particles, with molar composition $CaMn_{0.775}Ti_{0.125}Mg_{0.1}O_{3-\delta}$, have a perovskite structure where calcium, manganite, titanium and oxygen bind together and magnesium is present in a separate phase [55]. The Flemish Institute for

Technological Research (VITO), Belgium, manufactured the material from pro-analysis chemicals with a spray-drying technique. The particles, with a size range from 90 to 250 μm and a bulk density of 1300 kg m^{-3}, have been used in an earlier study focusing on alkali interactions in a laboratory-scale fluidized bed reactor, where material analysis with a scanning electron microscope was performed [29].

4. Results and discussion

The operational temperatures of the constructed experimental setup were initially evaluated. A thermocouple was submerged into the fluidized bed to ensure correct operating temperatures. The reactor was constructed using the results from CFD simulations as a guideline, and a bed temperature of 900 °C required an applied heat flux of 1820 W/m^2 in CFD simulations. This value is consistent with the operational parameters of the experimental setup including oven arrangement, which indicates that the parameters used in the simulations provide a qualitatively acceptable description of the setup. To not risk interaction with alkali, the thermocouple was removed prior to alkali injection to the reactor and placed on the lower flange outside the reactor body. The temperature in the upper reactor section experiencing ambient temperatures was also evaluated. The CFD results in Fig. 1a show that the wall temperature in the top section ranges from around 100 °C in the bottom, to room temperature further downstream. Measurements of the outer wall temperature on the upper reactor section confirmed the rapid decrease in temperature in this section and the main part of the section had a surface temperature below 60 °C.

Two types of experiments with alkali injection were conducted to evaluate the reactor performance under typical experimental conditions. In the first set of experiments, an empty reactor system was used to study the interaction between alkali and the inner reactor walls. The second set of experiments was carried out with a fluidized bed of OC particles in the reactor to study the interaction between alkali and the bed material. Temperatures from 160 to 900 °C were used in empty reactor experiments, and the operating temperatures were 800, 850 and 900 °C during the OC experiments. Experiments were carried out with a constant injection of either KOH or KCl aerosol particles in inert, reducing and oxidizing gas conditions to resemble the different stages of a CLC process. In most type of biomass, potassium is highly abundant and KOH and/or KCl are two of the major components that are being released to the gas phase during the fuel conversion process [4].

4.1. Influence of temperature in empty reactor

Fig. 5 shows the observed alkali concentrations in the empty reactor during constant KOH injection while incrementally increasing the temperature from 160 to 900 °C in inert, reducing and oxidizing conditions. The alkali concentration measured at the outlet is influenced by both the temperature and the gas conditions. The concentration decreases slowly as the temperature increases between 160 and 500 °C for all atmospheric conditions. Similar alkali concentrations are observed in inert and reducing conditions, while the concentration in oxidizing condition shows a similar temperature dependence but approximately 30% lower values (see Fig. 5a). At these relatively low temperatures, the injected alkali remain as aerosol particles, and losses likely originate from rapid particle diffusion in areas with large temperature gradients. With further increase in temperature, the alkali particles evaporate into their molecular constituents, resulting in a sharper drop in concentration. The sharp drop in outlet alkali concentration can be explained by greatly increased diffusion coefficients for gaseous alkali-containing compounds compared to alkali in the form of aerosol particles. With diffusion coefficients that are several orders of magnitude higher than those of aerosol particles, the alkali will rapidly diffuse to and interact with the inner walls of the empty reactor. The gaseous alkali concentration in the reactor will therefore depend on the balance between alkali adsorption by the wall and subsequently the alkali desorption from the wall at different temperatures. The lowest observed values were recorded at a reactor temperature of around 700 °C, before a slight

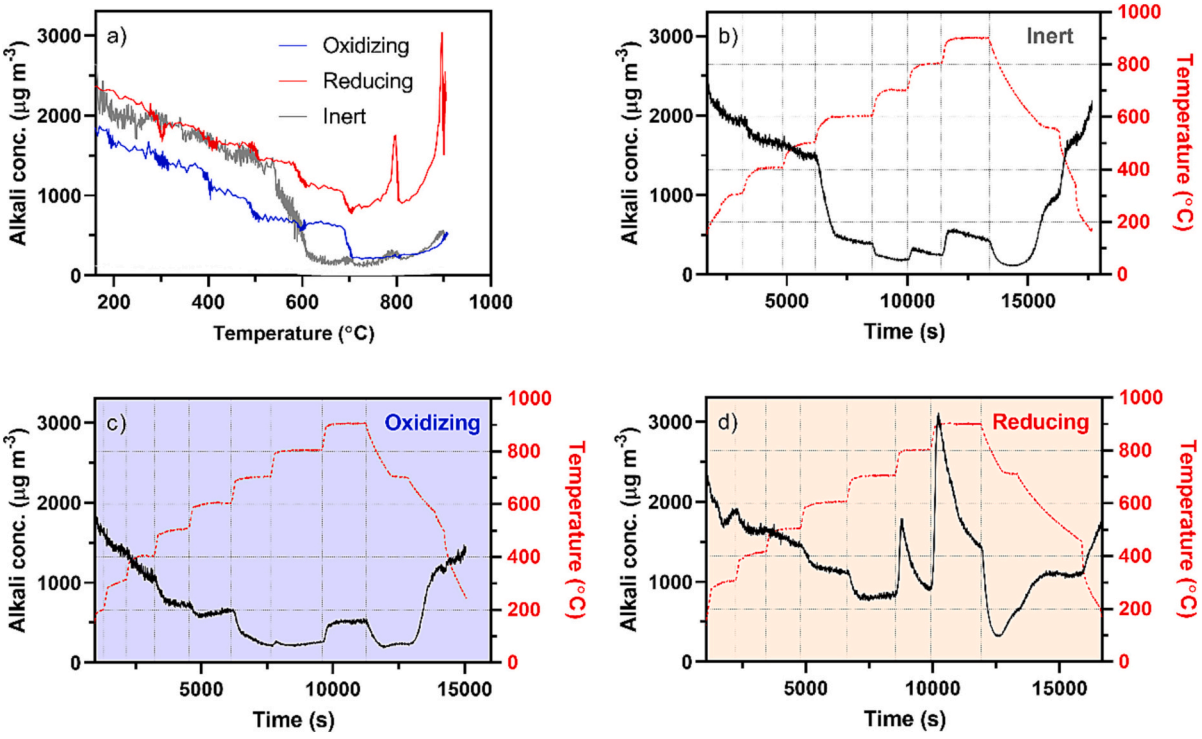

Fig. 5. (a) Measured alkali concentrations during constant KOH injection to an empty reactor as a function of temperature in inert (grey line), oxidizing (blue line), and reducing (red line) conditions. Alkali concentrations (black line) and reactor temperatures (red line) as a function of time in (b) inert, (c) oxidizing, and (d) reducing conditions. (For interpretation of the references to color in this figure legend, the reader is referred to the web version of this article.)

recovery was observed at the highest temperatures. The explanation being that more alkali can re-evaporate from the wall at higher temperatures, leading to higher outlet alkali concentrations. In the temperature range from 700 to 900 °C, the outlet concentrations of alkali under inert and oxidizing conditions were similar, whereas a considerably higher concentration was observed under reducing conditions. Observed differences between the results obtained in inert, reducing and oxidizing atmospheres may be due to several processes. The gas composition may affect the detailed composition of the surface layer of the wall, which in turn affects alkali-wall interactions in ways that are not fully understood. The gas composition may also affect the evaporation and decomposition of KOH particles, including their ability to form alkali oxides or carbonates. In addition, both aerosol and molecular diffusion processes are affected by the gas phase composition.

The temperature ramps in different gas conditions (Fig. 5b–d) show changes in alkali concentration as the temperature is raised in steps, reflecting differences in alkali-wall interactions depending on temperature and gas composition [29,32]. Raising the temperature from 700 to 800 °C in reducing conditions results in a transient increase in alkali concentration (Fig. 5d), which is followed by another transient increase when the temperature is further raised to 900 °C. These transients are not present in inert or oxidizing conditions (Fig. 5b and Fig. 5c), and indicate differences in alkali-wall interactions depending on gas composition.

4.2. Simulated CLC cycles

During a CLC process, the OC is transported in loop-seals between an AR and a FR. To simulate the OC circulation between oxidizing conditions in the AR, reducing conditions in the FR, and inert conditions in loop-seals, multiple redox cycles were performed in each CLC experiment. The cycle duration followed a specific pattern: 180 s in inert atmosphere, followed by 1000 s in reducing atmosphere, 500 s in inert atmosphere, and finally 1450 s in oxidizing atmosphere. The different durations were selected to allow complete oxidation or reduction of the OC during each stage, allow transients observed when changing gas composition to relax and approach a steady state concentration, and be comparable to the conditions used in an earlier study [29]. The longer residence time used in oxidizing conditions compared to reducing conditions is a consequence of the relatively low O_2 concentration used in the present study.

Fig. 6 shows the observed alkali and gas concentrations at reactor temperatures of 800, 850 and 900 °C with continuous KOH injection to (a) an empty reactor and (b) a fluidized bed of 20 g OC particles. Results are displayed from two consecutive redox cycles at each temperature, where colored fields mark recurring inert (white), reducing (orange) and oxidizing (blue) conditions. Large variations in outlet gas and alkali concentrations are observed within each redox cycle, and relatively high reproducibility is observed between the cycles. In the empty reactor the outlet alkali concentration increases with increasing temperature, and large transient changes in alkali concentration are seen when the gas composition changes. The relatively short time scales of these transients suggest that the processes are dominated by changes in alkali interactions with the outermost surface layer of the wall [32]. New steady state concentrations are established when the flow of alkali from the gas phase is balanced by alkali evaporation from the steel surface. The observed increase in concentration with temperature indicates an increased alkali evaporation rate from the wall at high temperatures.

The results with OC present show a distinctly different pattern compared to the empty reactor results. The alkali concentration still depends on gas composition with the highest concentrations observed under reducing conditions, but the concentrations are considerably lower. The temperature dependence of the alkali concentration is also less pronounced than observed in the empty reactor. The experimental results clearly show that the observed alkali concentration is strongly influenced by the presence of the OC fluidized bed. The kinetics of the alkali-OC interactions are also distinctly different compared to the kinetics of alkali-wall interactions in the empty reactor.

The alkali and gas concentrations during a single redox cycle are shown in greater detail in Fig. 6. The displayed results correspond to the second redox cycle at 900 °C (*i.e.,* cycle number 6 in Fig. 6). KOH interacts strongly with the inner steel wall in the empty reactor (black dashed line in Fig. 7). Shifting gas composition results in significant transient effects in alkali concentration that approaches steady conditions within a few hundred seconds. Notably, the transient behavior is especially significant when reducing conditions are applied, while switching between inert and oxidizing conditions has a substantially smaller effect. The presence of an OC fluidized bed (black solid line in Fig. 7) results in markedly different alkali behavior with lower concentrations compared to the empty reactor case. The alkali level changes with changing gas composition, but the transient behavior is generally smaller compared to the empty reactor case where alkali-wall interactions dominate the observed behavior. The different gas compositions affect the surface properties of the OC and changes in alkali level are observed during oxidation and reduction of the OC. In oxidizing conditions, the alkali concentration is lower after the OC oxidation

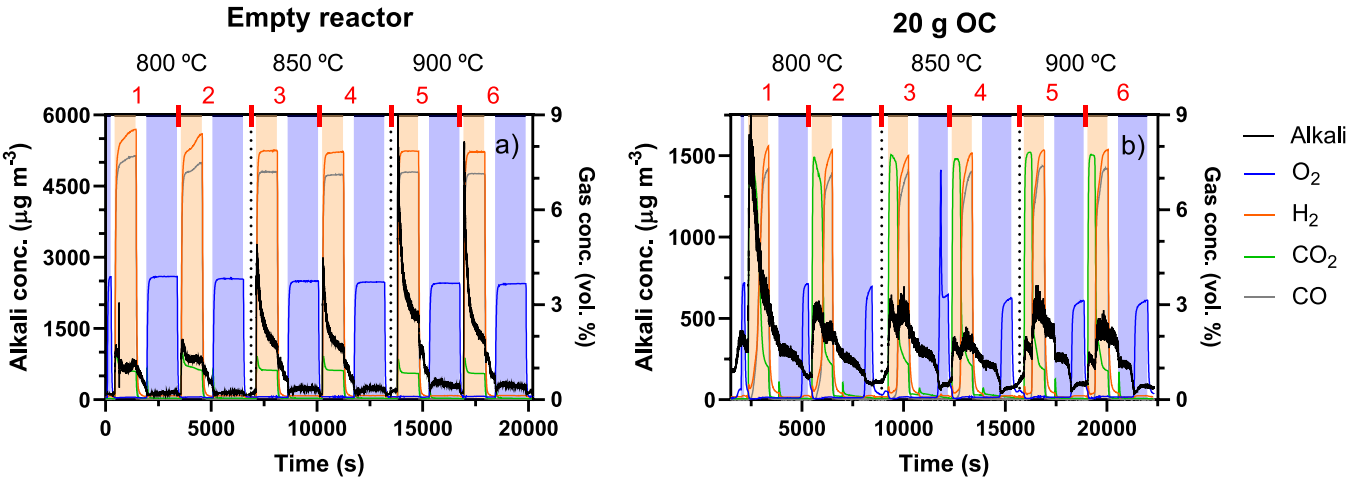

Fig. 6. Alkali and gas concentrations measured in the outlet from experiments with KOH aerosol: (a) an empty reactor and (b) a fluidized bed of 20 g OC particles present. The results show experiments from two consecutive redox cycles at 800, 850 and 900 °C where each cycle is marked in red. Colored fields mark periods with inert (white), reducing (orange) and oxidizing (blue) conditions. (For interpretation of the references to color in this figure legend, the reader is referred to the web version of this article.)

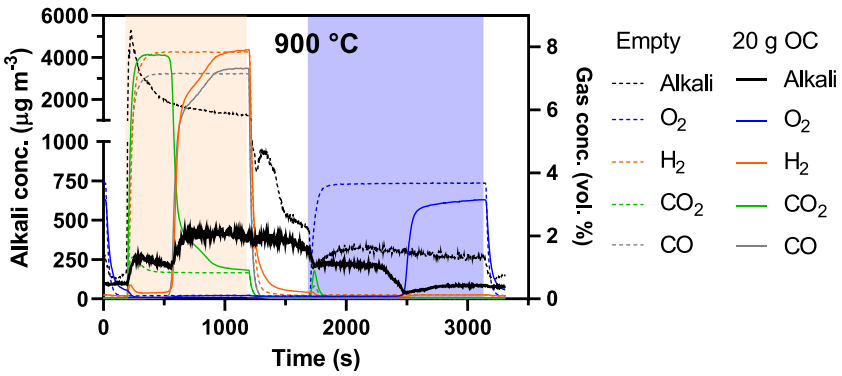

Fig. 7. Outlet alkali- and gas concentrations measured during one redox cycle in an empty reactor and a reactor containing OC at a reactor temperature of 900 °C and KOH aerosol injection. Colored areas mark stages with oxidizing (blue), inert (white) and reducing (orange) atmospheres. Black lines show alkali concentrations, and the colored lines show gas concentrations, where dashed and solid lines represent the empty reactor and OC experiments, respectively. (For interpretation of the references to color in this figure legend, the reader is referred to the web version of this article.)

process is completed compared to the initial 800 s when the OC bed undergoes oxidation. In reducing conditions the initial 400 s show the formation of CO_2, which mark the period where the OC undergoes reduction, and a lower alkali concentration is observed. After complete reduction of the OC bed the observed alkali concentration is generally higher.

In conclusion, the significant reduction in the outlet concentration of alkali when the fluidized bed is present, compared to the empty reactor experiment, suggests significant alkali uptake by the OC particles throughout the whole redox cycle at 900 °C.

4.3. Influence of fluidized bed inventory

To further evaluate the relative influence of hot reactor walls and OC material inventory on the results, experiments were carried out with different amounts of OC in the reactor. Fig. 8 shows the outlet alkali concentration measured during one redox cycle at 900 °C in an empty reactor and with a fluidized bed of 5, 10 or 20 g OC present in the reactor.

As described above, a major transient peak is observed under reducing conditions in the empty reactor. Addition of 5 g of OC has a major impact on the results and changes the qualitative behavior during the different stages of the redox cycle. The transient peak seen when applying reducing conditions disappears and the alkali concentration is lower than observed in the empty reactor in all stages. The same behavior is observed when using 10 and 20 g of OC, and the alkali concentration decreases with increasing size of the fluidized bed inventory.

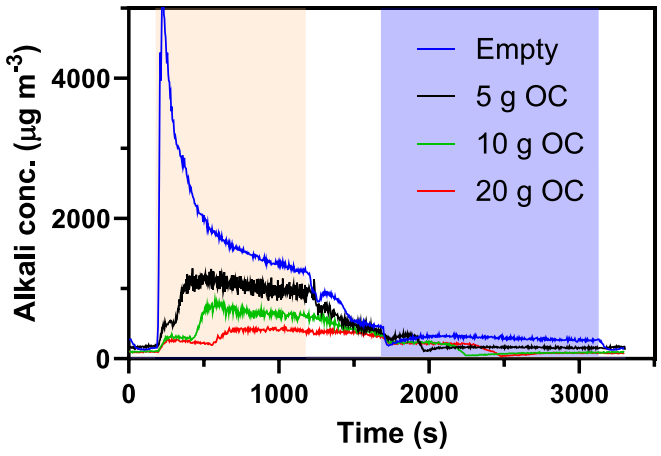

Fig. 8. Outlet alkali concentrations measured during one redox cycle with KOH injection to the reactor operated at 900 °C. The colors represent results for experiments with empty reactor (blue lines) and when the reactor is filled with 5 g OC (black lines), 10 g OC (green lines) and 20 g OC (red lines). Colored areas mark stages with oxidizing (blue), inert (white) and reducing (orange) atmospheres. (For interpretation of the references to color in this figure legend, the reader is referred to the web version of this article.)

The observations suggest that the OC results are dominated by alkali-OC interactions, and the influence of alkali-wall interactions is minor and decrease with the size of the inventory. To address the relative importance of the two types of surfaces available in the reactor, the total surface areas of the OC bed and the wall in the hot zone of the reactor may be estimated. The OC material has a BET specific surface area of 0.2 $m^2\ g^{-1}$ [56], and the total surface area of the 5, 10 and 20 g OC beds are approximately 1, 2 and 4 m^2, respectively. The hot zone of the reactor has a length of 200 mm and an inner diameter of 26 mm. This corresponds to a geometric total area of 0.016 m^3, which is 60–240 times smaller than the total surface areas of the fluidized beds. The actual surface of the wall is expected to be larger than the geometric area due to the microscopic structure of the wall material, but the inner surface area has not been experimentally determined.

It is concluded that the OC surface area is substantially larger than the wall area in the hot zone of the reactor, which is consistent with the large effects seen when introducing 5–20 g of OC to the reactor. The extensive wall interactions observed in the empty reactor experiments are thus unlikely to play a significant role when the reactor is filled with fluidized bed material. The use of a large amount of OC material reduces any effects of the wall and is thus beneficial in the experiments. In practice, the time required to oxidize and reduce the bed material during a redox cycle also needs to be taken into account when designing an experiment.

4.4. Influence of alkali species

Additional studies were carried out to evaluate the effects of the type of alkali species used in the experiments. Fig. 9 shows the outlet alkali concentrations in the presence and absence of 20 g OC present in the reactor at 800, 850 and 900 °C during constant injection of either KCl or KOH aerosol to the reactor. In empty reactor experiments (dotted lines in Fig. 9a and b), the outlet concentration of alkali increases with reactor temperature, and higher concentrations are observed during reducing conditions compared to oxidizing conditions. The most pronounced difference between KCl injection and KOH injection in the empty reactor experiments is seen when shifting from inert to reducing conditions. Shifting to reducing conditions, the KOH experiments shows peaks in the outlet alkali concentration, especially pronounced at the higher temperatures, while the KCl experiments show less pronounced transients. Apart from the initial stage of the reducing period, the observed alkali

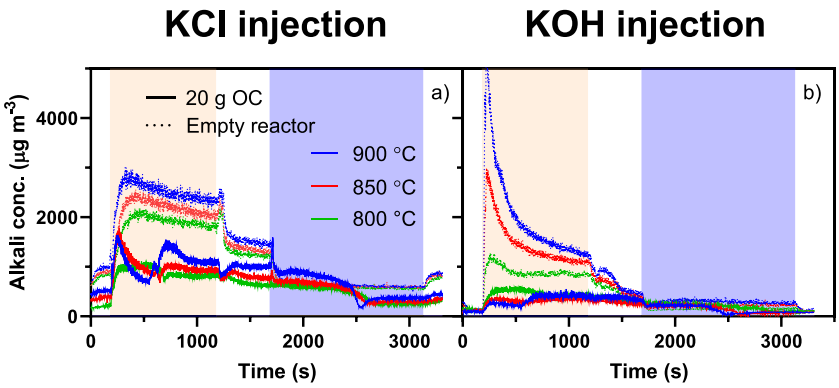

Fig. 9. Outlet alkali concentrations measured during one redox cycle with (a) KCl injection and (b) KOH injection to an empty reactor (dotted lines) and a reactor containing 20 g of OC (solid lines) at reactor temperatures of 800 (green lines), 850 (red lines) and 900 °C (blue lines). Colored areas mark stages with oxidizing (blue), inert (white) and reducing (orange) atmospheres. (For interpretation of the references to color in this figure legend, the reader is referred to the web version of this article.)

concentrations reach steady state after a few minutes, with slightly higher steady state alkali concentrations in the KCl experiments compared to the KOH experiments.

The presence of 20 g of fluidized OC in the reactor significantly influences the observed alkali concentrations (solid lines in Fig. 9a and b). The outlet alkali concentrations depend strongly on the oxidation and reduction of the OC material. The KCl experiments show significantly different behavior compared to KOH experiments when the OC undergoes reduction. In KCl experiments, the observed alkali concentration is generally higher during the first half of the reducing stage, compared to the second half of the reducing period where the OC is fully reduced, while the opposite is seen in KOH experiments. The results for KCl and KOH in oxidizing conditions are similar, with low outlet alkali concentrations in the beginning when the OC is being oxidized, and very low concentrations after the oxidation of the bed is completed.

The observed alkali uptake likely relates to chemical reactions between the alkali species and the OC surface, and it would require additional studies with detailed material analysis methods to identify the actual products. The same OC material was analyzed with scanning electron microscopy and energy-dispersive x-ray spectroscopy (SEM-EDX) before and after use in the previously employed reactor [29]. No significant changes in composition or morphology were observed after reactor experiments on similar time scales as used in the present study, which suggests that either longer operational times or higher alkali concentrations would be required to produce observable changes using SEM-EDX. Chemical changes may also involve the alkali species. KOH or KCl could undergo gas phase or surface reactions that change the counter ion, and thus the alkali species that interacts with the OC. Online experiments with a method that distinguishes between alkali species in the outflow from the reactor would be required to study these types of processes.

4.5. Comparison to previously used reactor

The main drawback of the reactor design previously used for alkali studies in CLC was the extensive alkali interactions with the reactor walls before and after the fluidized bed [32]. As a result, interactions with the reactor walls had to be taken into account during OC experiments [29]. In contrast, the reactor described here is designed to minimize alkali interactions with the walls above and below the fluidized bed. Fig. 10 shows a comparison between the observed alkali outlet concentration using the two types of laboratory reactors during operation at 850 °C and constant KCl injection. The empty reactor results displayed in Fig. 10a indicate significant differences between the reactors. The old reactor results (black line) shows three distinct transients: a sharp loss in alkali signal when reducing gases are turned on, a

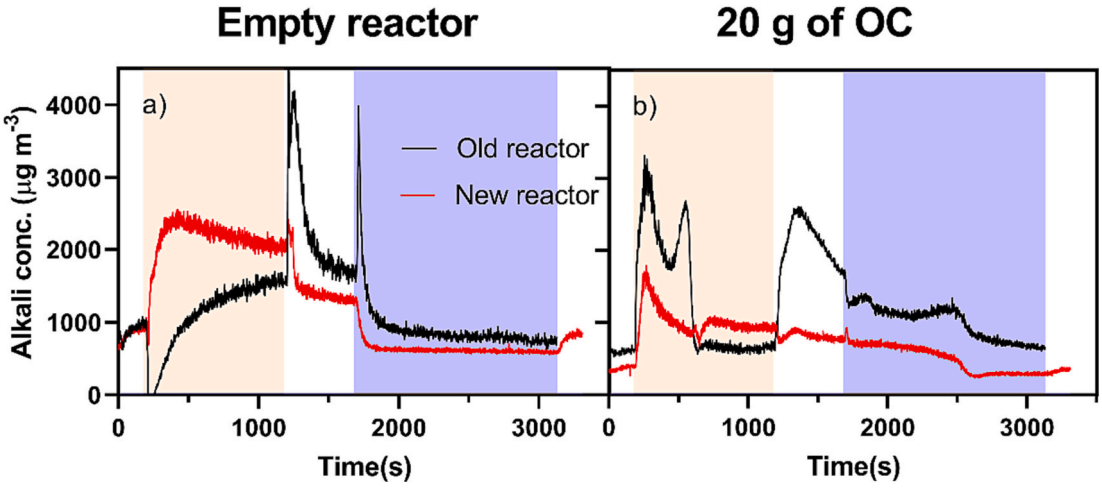

Fig. 10. Outlet alkali concentrations measured during one redox cycle at 850 °C reactor temperature with constant KCl injection to (a) empty reactor and (b) reactor filled with 20 g of OC. The colors represent results for experiments with the old laboratory reactor (black lines) and the new laboratory reactor presented in this study (red line). Colored areas mark stages with oxidizing (blue), inert (white) and reducing (orange) atmospheres. (For interpretation of the references to color in this figure legend, the reader is referred to the web version of this article.)

peak when shifting to inert conditions and another peak when oxidizing conditions are turned on. The new reactor (red line) lacks the transients in inert and oxidizing atmospheres, and the initial stage of the reducing period is characterized by a sharp increase in the alkali outlet concentration. The steady state concentrations approached towards the end of each stage of the redox cycle show similar alkali concentrations for both reactor systems. The hot section of the old and new reactor is built using different materials. The new material (Kanthal APMT™; Sandvik AB) was selected because it forms a stable surface oxide of non-scaling α-Al_2O_3 with good protection in corrosive high temperature environments, compared to Cr_2O_3 which is the main oxidation product of the stainless steel alloy used previously (alloy 316). Changes in surface properties are likely to affect how alkali binds to the surface of each material, and the higher stability of the new material may consequently be the reason for the less pronounced transient signals in the new reactor compared to the old one. Further studies with alternative methods will be required to determine the surface state of alkali under different conditions.

Fig. 10b shows experimental results when using 20 g of OC of the same type in each of the reactors. The observed alkali concentrations are qualitatively different for the two reactor systems, and the properties of the reactor clearly influence the results. The most obvious difference is seen in the inert conditions following the reducing stage. The results from the old reactor show a clear alkali peak during this period, while the new reactor results show a significantly more stable concentration, similar to the one seen before and after the inert gas was applied. Another major difference is seen in reducing conditions around the 500 s time mark where the old reactor shows a second peak in the alkali concentration, whereas this is not observed when using the new reactor.

This study demonstrates that the new reactor design represents an improvement over the previous reactor design used for similar alkali studies. One clear benefit of the new reactor is the absence of transients observed when changing gas composition in the empty reactor experiments (Fig. 10). Additionally, the surface area of the OC particles is significantly greater than that of the hot reactor walls in the new reactor, whereas in the old reactor, large areas of hot reactor walls above and below the fluidized bed interacted with the gaseous alkali and obscured the OC results. The results from the new reactor change consistently and systematically with changes in the oxidation state of the bed material during the redox cycle in experiments with different alkali species at different temperatures (Fig. 9). Experiments also show that addition of only 5 g of OC is sufficient to qualitative change the behavior compared to an empty reactor (Fig. 8), indicating a limited influence of the reactor walls. Minor effects of the reactor walls may still remain in the new setup, and should be carefully considered as the reactor is applied in studies of new alkali-OC systems. It is likely that alkali-OC systems with different behavior than the ones used here will contribute to an improved understanding. In addition, the development will benefit from characterization of alkali-surface interactions with alternative methods that constrain the potential outcomes.

5. Conclusions

A novel laboratory-scale fluidized bed reactor has been designed and constructed for alkali-related studies in conditions relevant to CLC. The geometric configuration is based on CFD simulations in combination with basic knowledge about the behavior of aerosol particles at high temperatures. The reactor is designed to minimize alkali losses before and after a fluidized bed, and to study the interactions between gaseous alkali and solid bed particles. The function of the reactor was demonstrated with a few typical CLC experiments with a constant alkali injection to *i)* an empty reactor, and *ii)* a fluidized bed of OC present in the reactor, while the alkali and gas concentrations were measured online in the exhaust gases. The OC material consisted of calcium manganite perovskite ($CaMn_{0.775}Ti_{0.125}Mg_{0.1}O_{3-\delta}$) and the alkali was continuously fed as KOH or KCl aerosol particles. Alkali interactions were investigated at temperatures up to 900 °C in reducing, inert and oxidizing conditions. The main conclusions are:

- The experimental set-up facilitates continuous alkali injection to the reactor system, where the operational parameters can be changed easily to study their effects on the interactions between gaseous alkali and a fluidized bed of solid particles.
- When operated without a fluidized bed present, empty reactor experiments show considerable wall effects, with the highest alkali losses to the walls observed at 700 °C in inert and oxidizing conditions.
- With a fluidized bed present, the surface area of the OC is one to two orders of magnitude larger than the surface area of the hot reactor walls, which makes alkali-wall interactions less important.
- Alkali uptake by the OC is characterized in all conditions, and observed to depend on gas composition, reactor temperature and type of alkali compound.

It is concluded that the newly designed laboratory reactor outperforms previous reactors used in these types of alkali studies. The development opens up for detailed studies of alkali-OC interactions under different operational conditions, and future work will include studies using different alkali species such as alkali chlorides and hydroxides and other types of OC materials to better understand the underlying processes. The novel designs of the inlet and outlet regions of the reactor presented here may also be applied to other types of fixed or fluidised bed reactors where condensation on reactor walls is an issue.

ORCID

Viktor Andersson: 0000-0001-5378-2892
Xiangrui Kong: 0000-0002-7205-0723
Henrik Leion: 0000-0002-9716-2553
Tobias Mattisson: 0000-0003-3942-7434
Jan Pettersson: 0000-0001-8420-6126

CRediT author statement

Viktor Andersson: Investigation, Formal analysis, Methodology, Resources, Writing- Original draft preparation, Writing- Reviewing and Editing.

Xiangrui Kong: Supervision, Writing- Reviewing and Editing.

Henrik Leion: Supervision, Resources, Writing- Reviewing and Editing.

Tobias Mattisson: Supervision, Writing- Reviewing and Editing.

Jan B. C. Pettersson: Conceptualization, Formal analysis, Supervision, Resources, Writing- Reviewing and Editing.

Declaration of Competing Interest

The authors declare that they have no known competing financial interests or personal relationships that could have appeared to influence the work reported in this paper.

Data availability

Data will be made available on request.

Acknowledgments

This work is supported by the Swedish Research Council, project “Biomass combustion chemistry with oxygen carriers” 2016-06023.

References

[1] J. Adánez, A. Abad, T. Mendiara, P. Gayán, L.F. de Diego, F. García-Labiano, Chemical looping combustion of solid fuels, Prog. Energy Combust. Sci. 65 (2018) 6–66, https://doi.org/10.1016/j.pecs.2017.07.005.

[2] A. Lyngfelt, Chemical looping combustion: status and development challenges, Energy Fuel 34 (8) (2020) 9077–9093, https://doi.org/10.1021/acs.energyfuels.0c01454.

[3] A. Lyngfelt, B. Leckner, T. Mattisson, A fluidized-bed combustion process with inherent CO2 separation; application of chemical-looping combustion, Chem. Eng. Sci. 56 (10) (2001) 3101–3113, https://doi.org/10.1016/S0009-2509(01)00007-0.

[4] M. Zevenhoven, P. Yrjas, M. Hupa, Ash-Forming Matter and Ash-Related Problems, 2010, https://doi.org/10.1002/9783527628148.hoc068.

[5] I. Gogolev, C. Linderholm, D. Gall, M. Schmitz, T. Mattisson, et al., Chemical-looping combustion in a 100 kW unit using a mixture of synthetic and natural oxygen carriers – Operational results and fate of biomass fuel alkali, Int. J. Greenhouse Gas Control 88 (2019) 371–382, https://doi.org/10.1016/j.ijggc.2019.06.020.

[6] R.P.W.J. Struis, C. von Scala, S. Stucki, R. Pins, Gasification reactivity of charcoal with C02 at elevated conversion levels, in: Progress in Thermochemical Biomass Conversion, 2001, pp. 73–91, https://doi.org/10.1002/9780470694954.ch5.

[7] H. Yang, S. Kudo, K. Norinaga, J.-i. Hayashi, Steam–oxygen gasification of potassium-loaded lignite: proof of concept of type IV gasification, Energy Fuel 30 (3) (2016) 1616–1627, https://doi.org/10.1021/acs.energyfuels.5b02258.

[8] A.A. Khan, W. de Jong, P.J. Jansens, H. Spliethoff, Biomass combustion in fluidized bed boilers: potential problems and remedies, Fuel Process. Technol. 90 (1) (2009) 21–50, https://doi.org/10.1016/j.fuproc.2008.07.012.

[9] E. Hupa, E. Vainio, P. Yrjas, M. Engblom, M. Hupa, Corrosion of superheater materials by alkali chloride salt mixtures-the role of the presence of molten phase, FUEL 344 (2023), https://doi.org/10.1016/j.fuel.2023.128063.

[10] J.-E. Eriksson, M. Zevenhoven, P. Yrjas, A. Brink, L. Hupa, Corrosion of heat transfer materials by potassium-contaminated ilmenite bed particles in chemical-looping combustion of biomass, Energies 15 (8) (2022) 2740, https://doi.org/10.3390/en15082740.

[11] A. Corcoran, J. Marinkovic, F. Lind, H. Thunman, P. Knutsson, M. Seemann, Ash properties of ilmenite used as bed material for combustion of biomass in a circulating fluidized bed boiler, Energy Fuel 28 (12) (2014) 7672–7679, https://doi.org/10.1021/ef501810u.

[12] I. Staničić, V. Andersson, M. Hanning, T. Mattisson, R. Backman, H. Leion, Combined manganese oxides as oxygen carriers for biomass combustion — ash interactions, Chem. Eng. Res. Des. 149 (2019) 104–120, https://doi.org/10.1016/j.cherd.2019.07.004.

[13] M. Öhman, A. Nordin, B.-J. Skrifvars, R. Backman, M. Hupa, Bed agglomeration characteristics during fluidized bed combustion of biomass fuels, Energy Fuel 14 (1) (2000) 169–178, https://doi.org/10.1021/ef990107b.

[14] Z.-M. He, J.-P. Cao, X.-Y. Zhao, Review of biomass agglomeration for fluidized-bed gasification or combustion processes with a focus on the effect of alkali salts, Energy Fuel 36 (16) (2022) 8925–8947, https://doi.org/10.1021/acs.energyfuels.2c01183.

[15] W. Zhang, X. Liu, G. Xu, T. Song, Sulfur evolution and capture behavior by a solid waste of red mud during chemical looping combustion of petroleum coke, Energy Fuel 36 (19) (2022) 12104–12115, https://doi.org/10.1021/acs.energyfuels.2c02154.

[16] J. Yu, Q. Guo, Y. Gong, L. Ding, J. Wang, G. Yu, A review of the effects of alkali and alkaline earth metal species on biomass gasification, Fuel Process. Technol. 214 (2021), 106723, https://doi.org/10.1016/j.fuproc.2021.106723.

[17] S. Anis, Z.A. Zainal, Tar reduction in biomass producer gas via mechanical, catalytic and thermal methods: a review, Renew. Sustain. Energy Rev. 15 (5) (2011) 2355–2377, https://doi.org/10.1016/j.rser.2011.02.018.

[18] K. Mitsuoka, S. Hayashi, H. Amano, K. Kayahara, E. Sasaoaka, M.A. Uddin, Gasification of woody biomass char with CO2: the catalytic effects of K and Ca species on char gasification reactivity, Fuel Process. Technol. 92 (1) (2011) 26–31, https://doi.org/10.1016/j.fuproc.2010.08.015.

[19] Y. Ge, S. Ding, W. Zhang, X. Kong, K. Engvall, J.B.C. Pettersson, Effect of fresh bed materials on alkali release and thermogravimetric behavior during straw gasification, Fuel 336 (2023), 127143, https://doi.org/10.1016/j.fuel.2022.127143.

[20] J. Wei, X. Song, Q. Guo, L. Ding, K. Yoshikawa, G. Yu, Reactivity, synergy, and kinetics analysis of CO2 co-pyrolysis/co-gasification of biomass after hydrothermal treatment and coal blends, Energy Fuel 34 (1) (2020) 294–303, https://doi.org/10.1021/acs.energyfuels.9b03721.

[21] Y.X. Ge, S.M. Ding, X.R. Kong, E. Kantarelis, K. Engvall, J.B.C. Pettersson, Real-time monitoring of alkali release during CO2 gasification of different types of biochar, Fuel 327 (2022), https://doi.org/10.1016/j.fuel.2022.125102.

[22] C. Dupont, T. Nocquet, J.A. Da Costa, C. Verne-Tournon, Kinetic modelling of steam gasification of various woody biomass chars: influence of inorganic elements, Bioresour. Technol. 102 (20) (2011) 9743–9748, https://doi.org/10.1016/j.biortech.2011.07.016.

[23] C. Dupont, S. Jacob, K.O. Marrakchy, C. Hognon, M. Grateau, et al., How inorganic elements of biomass influence char steam gasification kinetics, Energy 109 (2016) 430–435, https://doi.org/10.1016/j.energy.2016.04.094.

[24] O. Karlström, M.J. Dirbeba, M. Costa, A. Brink, M. Hupa, Influence of K/C ratio on gasification rate of biomass chars, Energy Fuel 32 (10) (2018) 10695–10700, https://doi.org/10.1021/acs.energyfuels.8b02288.

[25] T. Suzuki, H. Nakajima, N.-o. Ikenaga, H. Oda, T. Miyake, Effect of mineral matters in biomass on the gasification rate of their chars, Biomass Conv. Biorefine. 1 (1) (2011) 17–28, https://doi.org/10.1007/s13399-011-0006-2.

[26] T. Mendiara, A. Abad, L.F. de Diego, F. García-Labiano, P. Gayán, J. Adánez, Biomass combustion in a CLC system using an iron ore as an oxygen carrier, Int. J. Greenhouse Gas Control 19 (2013) 322–330, https://doi.org/10.1016/j.ijggc.2013.09.012.

[27] E. Darwish, D. Yılmaz, H. Leion, Experimental and thermodynamic study on the interaction of copper oxygen carriers and oxide compounds commonly present in ashes, Energy Fuel 33 (3) (2019) 2502–2515, https://doi.org/10.1021/acs.energyfuels.8b04060.

[28] D. Gall, M. Pushp, A. Larsson, K. Davidsson, J.B.C. Pettersson, Online measurements of alkali metals during start-up and operation of an industrial-scale biomass gasification plant, Energy Fuel 32 (1) (2018) 532–541, https://doi.org/10.1021/acs.energyfuels.7b03135.

[29] V. Andersson, A.H. Soleimanisalim, X. Kong, H. Leion, T. Mattisson, J.B.C. Pettersson, Alkali interactions with a calcium manganite oxygen carrier used in chemical looping combustion, Fuel Process. Technol. 227 (2022), 107099, https://doi.org/10.1016/j.fuproc.2021.107099.

[30] M. Pushp, D. Gall, K. Davidsson, M. Seemann, J.B.C. Pettersson, Influence of bed material, additives, and operational conditions on alkali metal and tar concentrations in fluidized bed gasification of biomass, Energy Fuel 32 (6) (2018) 6797–6806, https://doi.org/10.1021/acs.energyfuels.8b00159.

[31] A. Gyllén, P. Knutsson, F. Lind, H. Thunman, Magnetic separation of ilmenite used as oxygen carrier during combustion of biomass and the effect of ash layer buildup on its activity and mechanical strength, Fuel 269 (2020), 117470, https://doi.org/10.1016/j.fuel.2020.117470.

[32] V. Andersson, A.H. Soleimanisalim, X. Kong, F. Hildor, H. Leion, et al., Alkali-wall interactions in a laboratory-scale reactor for chemical looping combustion studies, Fuel Process. Technol. 217 (2021), 106828, https://doi.org/10.1016/j.fuproc.2021.106828.

[33] F. Hildor, M. Zevenhoven, A. Brink, L. Hupa, H. Leion, Understanding the interaction of potassium salts with an ilmenite oxygen carrier under dry and wet conditions, ACS Omega 5 (36) (2020) 22966–22977, https://doi.org/10.1021/acsomega.0c02538.

[34] F. Störner, F. Hildor, H. Leion, M. Zevenhoven, L. Hupa, M. Rydén, Potassium ash interactions with oxygen carriers steel converter slag and iron mill scale in chemical-looping combustion of biomass—experimental evaluation using model compounds, Energy Fuel 34 (2) (2020) 2304–2314, https://doi.org/10.1021/acs.energyfuels.9b03616.

[35] M. Zevenhoven, C. Sevonius, P. Salminen, D. Lindberg, A. Brink, et al., Defluidization of the oxygen carrier ilmenite – laboratory experiments with potassium salts, Energy 148 (2018) 930–940, https://doi.org/10.1016/j.energy.2018.01.184.

[36] C. Sevonius, P. Yrjas, D. Lindberg, L. Hupa, Impact of sodium salts on agglomeration in a laboratory fluidized bed, Fuel 245 (2019) 305–315, https://doi.org/10.1016/j.fuel.2019.02.034.

[37] Z. Zhang, J. Liu, F. Shen, Z. Wang, Temporal release behavior of potassium during pyrolysis and gasification of sawdust particles, Renew. Energy 156 (2020) 98–106, https://doi.org/10.1016/j.renene.2020.04.076.

[38] W.C. Hinds, Aerosol Technology - Properties, Behavior and Measurement of Airborne Particles, Wiley, New York, 1999.

[39] Z. Hu, X. Wang, Y. Zhou, H. Wu, P. Glarborg, H. Tan, Assessment of the effect of alkali chemistry on post-flame aerosol formation during oxy-combustion of biomass, Fuel 311 (2022), 122521, https://doi.org/10.1016/j.fuel.2021.122521.

[40] A.M. Huntz, A. Reckmann, C. Haut, C. Sévérac, M. Herbst, et al., Oxidation of AISI 304 and AISI 439 stainless steels, Mater. Sci. Eng. A 447 (1) (2007) 266–276, https://doi.org/10.1016/j.msea.2006.10.022.

[41] T. Jonsson, H. Larsson, S. Karlsson, H. Hooshyar, M. Sattari, et al., High-temperature oxidation of FeCr(Ni) alloys: the behaviour after breakaway, Oxidation Metals 87 (3) (2017) 333–341, https://doi.org/10.1007/s11085-017-9731-7.

[42] S.C. Cha, M. Spiegel, Local reactions of KCl particles with iron, nickel and chromium surfaces, Mater. Corros. 57 (2) (2006) 159–164, https://doi.org/10.1002/maco.200503903.

[43] J. Pettersson, J.E. Svensson, L.G. Johansson, KCl-induced corrosion of a 304-type austenitic stainless steel in O2 and in O2 + H2O environment: the influence of temperature, Oxid. Met. 72 (3) (2009) 159–177, https://doi.org/10.1007/s11085-009-9153-2.

[44] K. Gosiewski, A. Pawlaczyk-Kurek, Aerodynamic CFD simulations of experimental and industrial thermal flow reversal reactors, Chem. Eng. J. 373 (2019) 1367–1379, https://doi.org/10.1016/j.cej.2019.03.274.

[45] D.I. Pashchenko, CFD modeling of operating processes of a solar air heater in ANSYS FLUENT, J. Eng. Phys. Thermophys. 92 (1) (2019) 73–79, https://doi.org/10.1007/s10891-019-01908-8.

[46] S. Li, Y. Shen, An approach to simulate gas-solid flow systems with process controllers, Chem. Eng. J. 429 (2022), 132443, https://doi.org/10.1016/j.cej.2021.132443.

[47] A. Inc, Pressure-Velocity Coupling, ANSYS FLUENT 12.0 Theory Guide. https://www.afs.enea.it/project/neptunius/docs/fluent/html/th/node373.htm, 2009 (Accessed 2023-09-04 2023).

[48] A. Inc, Choosing the Pressure-Velocity Coupling Method, ANSYS FLUENT 12.0 User's Guide. https://www.afs.enea.it/project/neptunius/docs/fluent/html/ug/node785.htm#sec-uns-solve-pvel, 2009 (Accessed 2023-09-04 2023).

[49] N. Israelsson, J. Engkvist, K. Hellström, M. Halvarsson, J.E. Svensson, L. G. Johansson, KCl-induced corrosion of an FeCrAl alloy at 600 °C in O2 + H2O

environment: the effect of pre-oxidation, Oxidation Metals 83 (1) (2015) 29–53, https://doi.org/10.1007/s11085-014-9507-2.
[50] M. Hagström, K. Engvall, J.B.C. Pettersson, Desorption kinetics at atmospheric pressure: alkali metal ion emission from hot platinum surfaces, J. Phys. Chem. B. 104 (18) (2000) 4457–4462, https://doi.org/10.1021/jp000311w.
[51] K. Davidsson, K. Engvall, M. Hagström, J. Korsgren, B. Lönn, J. Pettersson, A surface ionization instrument for on-line measurements of alkali metal components in combustion: instrument description and applications, Energ Fuel 16 (2002), https://doi.org/10.1021/ef020020h.
[52] V. Andersson, Y. Ge, X. Kong, J.B.C. Pettersson, A novel method for on-line characterization of alkali release and thermal stability of materials used in thermochemical conversion processes, Energies 15 (12) (2022) 4365, https://doi.org/10.3390/en15124365.
[53] D. Gall, J. Viljanen, I. Gogolev, T. Allgurén, K. Andersson, Alkali monitoring of industrial process gas by surface ionization—calibration, assessment, and comparison to in situ laser diagnostics, Energy Fuel (2021), https://doi.org/10.1021/acs.energyfuels.1c03205.
[54] I. Gogolev, A.H. Soleimanisalim, C. Linderholm, A. Lyngfelt, Commissioning, performance benchmarking, and investigation of alkali emissions in a 10 kWth solid fuel chemical looping combustion pilot, Fuel 287 (2021), 119530, https://doi.org/10.1016/j.fuel.2020.119530.
[55] P. Hallberg, M. Hanning, M. Rydén, T. Mattisson, A. Lyngfelt, Investigation of a calcium manganite as oxygen carrier during 99h of operation of chemical-looping combustion in a 10kWth reactor unit, Int. J. Greenhouse Gas Control 53 (2016) 222–229, https://doi.org/10.1016/j.ijggc.2016.08.006.
[56] D. Jing, M. Jacobs, P. Hallberg, A. Lyngfelt, T. Mattisson, Development of CaMn0.775Mg0.1Ti0.125O3-δ oxygen carriers produced from different Mn and Ti sources, Mater. Des. 89 (2016) 527–542, https://doi.org/10.1016/j.matdes.2015.09.117.